Article

0.68% of solar-to-hydrogen efficiency and high photostability of organic-inorganic membrane catalyst

Wei Li [1] ✉, Wen Duan[1], Guocheng Liao[1], Fanfan Gao[1], Yusen Wang[1], Rongxia Cui[1], Jincai Zhao [2] & Chuanyi Wang [3] ✉

Solar-driven flat-panel H_2O-to-H_2 conversion is an important technology for value-added solar fuel production. However, most frequently used particulate photocatalysts are hard to achieve stable photocatalysis in flat-panel reaction module due to the influence of mechanical shear force. Herein, a highly active $CdS@SiO_2$-Pt composite with rapid CdS-to-Pt electron transfer and restrained photoexciton recombination was prepared to process into an organic-inorganic membrane by compounding with polyvinylidene fluoride (PVDF). This PVDF networked organic-inorganic membrane displays high photo-stability and excellent operability, achieving improved simulated sunlight-driven alkaline H_2O-to-H_2 conversion activity (213.48 mmol m^{-2} h^{-1}) following a 0.68% of solar-to-hydrogen efficiency. No obvious variation in its appearance and micromorphology was observed even being recycled for 50-times, which considerably outperforms the existing membrane photocatalysts. Subsequently, a homemade panel H_2O-to-H_2 conversion system was fabricated to obtain a 0.05% of solar-to-hydrogen efficiency. In this study, we opens up a prospect for practical application of photocatalysis technology.

In recent years, solar-driven photocatalytic technology has been identified as a prospective strategy to solve the issues of environmental hazards and energy shortage[1]. Particularly, the photovoltaic H_2O-to-H_2 (HTH) conversion technique has widely attracted the research interest of many scholars in the context of carbon neutrality[2]. However, low photon conversion efficiency in green hydrogen production is a nonnegligible technical obstacle limiting its practical application. Therefore, a large number of high-performance photocatalysts have been developed for various applications, such as pollutant remediation[3], water splitting[4], CO_2 reduction[5], nitrogen fixation[6], hydrogen peroxide production[7], alkane conversion[8], etc. However, most of reported photocatalysts are micro/nano-scale inorganic particulate materials, which require ultrasonic dispersion in catalytic process following a filtration or centrifugation to achieve its

recovery, thus it is difficult to meet the requirement of practical applications due to the shortcomings of unstable microstructure, energy-extensive consumption, cumbersome operation, high cost, etc.

Immobilizing particulate photocatalysts on large-sized substrate (e.g., SiO_2, hydrotalcite, ITO glass, polymer, etc.) can effectively improve its stability and acquire easier separation/recovery ability[9,10]. In view of the light dependence of photocatalyst, it has been proposed to modularize into a flat panel for indefinitely expansion, so as to realize large-scale application of photocatalytic technology[11]. For example, Domen's team developed a panel reaction system based on Al-doped $SrTiO_3$ photocatalyst for building of a 100-m^2 scaled solar-to-hydrogen (STH) energy conversion system[12]. Subsequently, Mi et al. built a panel water-splitting system based on InGaN photocatalyst[13]. Generally, particulate photocatalysts were immobilized on flat-panel

[1]College of Chemistry and Chemical Engineering, Shaanxi Key Laboratory of Chemical Additives for Industry, Shaanxi University of Science and Technology, Xi'an, Shaanxi, China. [2]Key Laboratory of Photochemistry, Beijing National Laboratory for Molecular Sciences, Institute of Chemistry, Chinese Academy of Sciences, Beijing, PR China. [3]School of Environmental Sciences and Engineering, Shaanxi University of Science and Technology, Xi'an, Shaanxi, China. ✉e-mail: liweihg@sust.edu.cn; wangchuanyi@sust.edu.cn

reaction module with the aid of adhesives (e.g., Nafion), it is easy to lose from the flat panel due to mechanical shear force influence of fluid and generated bubbles, resulting a decreased photoactivity. Moreover, single light-driven dynamics has obvious limitations for obtaining higher activity. On the one hand, it is difficult to generate higher-density photoexcitons. On the other hand, high-frequency photoexciton recombination greatly decreases photon utilization efficiency. Multi-field-driven catalysis can greatly overcome the obstacles of photocatalysis due to its merits of diversified excitation sources and faster exciton separation kinetics[14].

Piezoelectric-photocatalysis is an emerging research topic developed in photocatalysis field in recent years[15]. For instance, Chen et al. found the piezoelectricity of 2D wrinkled WS_2 monolayers by forming regions of high and low tensile strain, obtaining enhanced hydrogen production activity due to faster exciton separation[16]. Lan et al. utilized the synergistic effect between polarized electric field and photo-carriers to obtain more efficient catalytic overall water splitting performance[17]. Compared with inorganic ferroelectric materials, polyvinylidene fluoride (PVDF), an organic ferroelectric material with high sensitivity of non-ultrasonic and low-frequency vibration, appears higher piezoelectric coefficient (especially the β, γ, δ phases) due to its strong polarity originated from the parallel molecular accumulation[18]. Moreover, in view of the merits of flexibility, chemical inertia, non-toxicity, etc., it is easy to be processed into fabric membrane structure through a simple polymer processing technique to obtain better operability[19]. If it is compounded with micro/nano sized inorganic photocatalysts to construct organic-inorganic composites, superior extended features (e.g., good regenerability and structural stability) can be obtained. Meanwhile, its good fluid mechanical energy sensitivity can integrate the merits of piezoelectric catalysis and photocatalysis, realizing multi-field-driven catalysis based on light energy and mechanical energy, obtaining highly improved catalytic activity.

In this work, a highly active $CdS@SiO_2$-Pt composite with rapid CdS-to-Pt electron-transfer kinetics and restrained photoexciton recombination kinetics was prepared to process into an organic-inorganic membrane by compounding with organic ferroelectric PVDF. This PVDF networked membrane catalyst with synergistic organic-inorganic interface displays high photostability and excellent operability, dramatically overcoming the drawback of inorganic particulate catalysts, and achieving improved simulated sunlight (SSL)-driven alkaline (pH = 14.0) HTH activity with unconspicuous variation in its appearance and micromorphology after 50-times of cycles. Subsequently, a homemade panel reaction system was fabricated to drive alkaline water-splitting under SSL-irradiation. This study opens up a prospect for practical application of panel photocatalytic hydrogen production with organic-inorganic interface networked membrane technology.

Results and discussion

Microstructure, topology and photoactivity of $CdS@SiO_2$-Pt photocatalyst

SiO_2 nanolayer was coated on the surface of CdS NRs to prepare the $CdS@SiO_2$ NRs via a sol-gel method (Fig. 1a). Fourier transform infrared (FTIR) spectrum in Supplementary Fig. 1 shows strong absorption peaks assigned to the anti-symmetric stretching vibration of Si-O-Si bonds and bending vibration of Si-O bonds at $1080\ cm^{-1}$ and $790\ cm^{-1}$[20]. Its high-resolution Si 2p and O 1s XPS spectra in Supplementary Fig. 2a, b respectively show a single characteristic peak at binding energy of 101.35 eV and two characteristic peaks at binding energies of 530.38 eV and 531.74 eV, which can be assigned to Si 2p electron orbital of SiO_2[21] and exposed silicon hydroxyl groups and Si-O bonds[22,23]. Moreover, its X-ray diffraction (XRD) pattern in Fig. 1b still appear the crystal characteristic of hexagonal CdS (PDF#77-2306)[24] without the observation of other crystal phases, and the typical diffraction corresponding to amorphous SiO_2 is not observed around 2θ = 24°. Above results indicate that a small amount of SiO_2 was successfully coated on the surface of CdS NRs, and transmission electron microscope (TEM) and high-resolution TEM (HRTEM) images in Fig. 1c
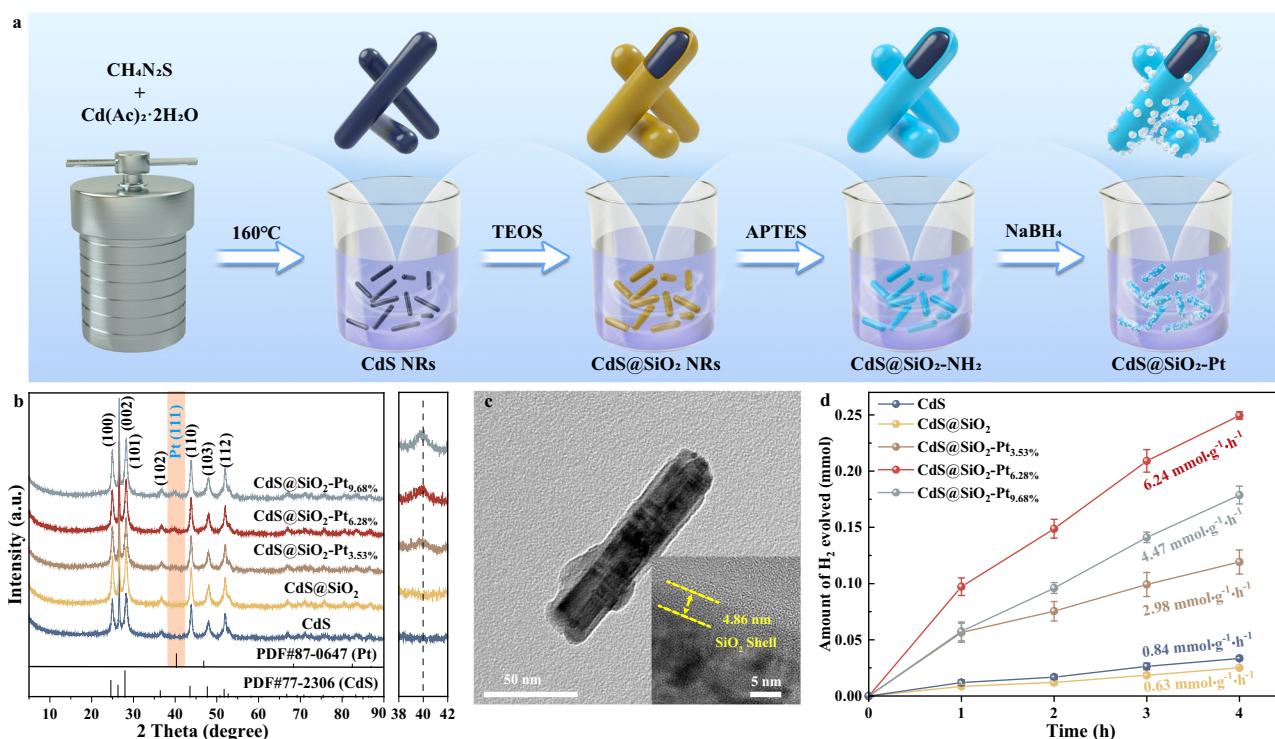

Fig. 1 | The preparation, microstructure and photoactivity of $CdS@SiO_2$-Pt photocatalyst. a Preparation diagram of $CdS@SiO_2$-Pt photocatalyst. **b** XRD patterns and (**d**), HTH conversion performances of CdS NRs, $CdS@SiO_2$ NRs and $CdS@SiO_2$-Pt photocatalysts with different Pt loading capacities (3.53%, 6.28%, 9.68%). **c** TEM images of $CdS@SiO_2$ NRs. The inset of (**c**) is the partial magnification. Error bars in (**d**) indicate the standard deviation for three measurements.
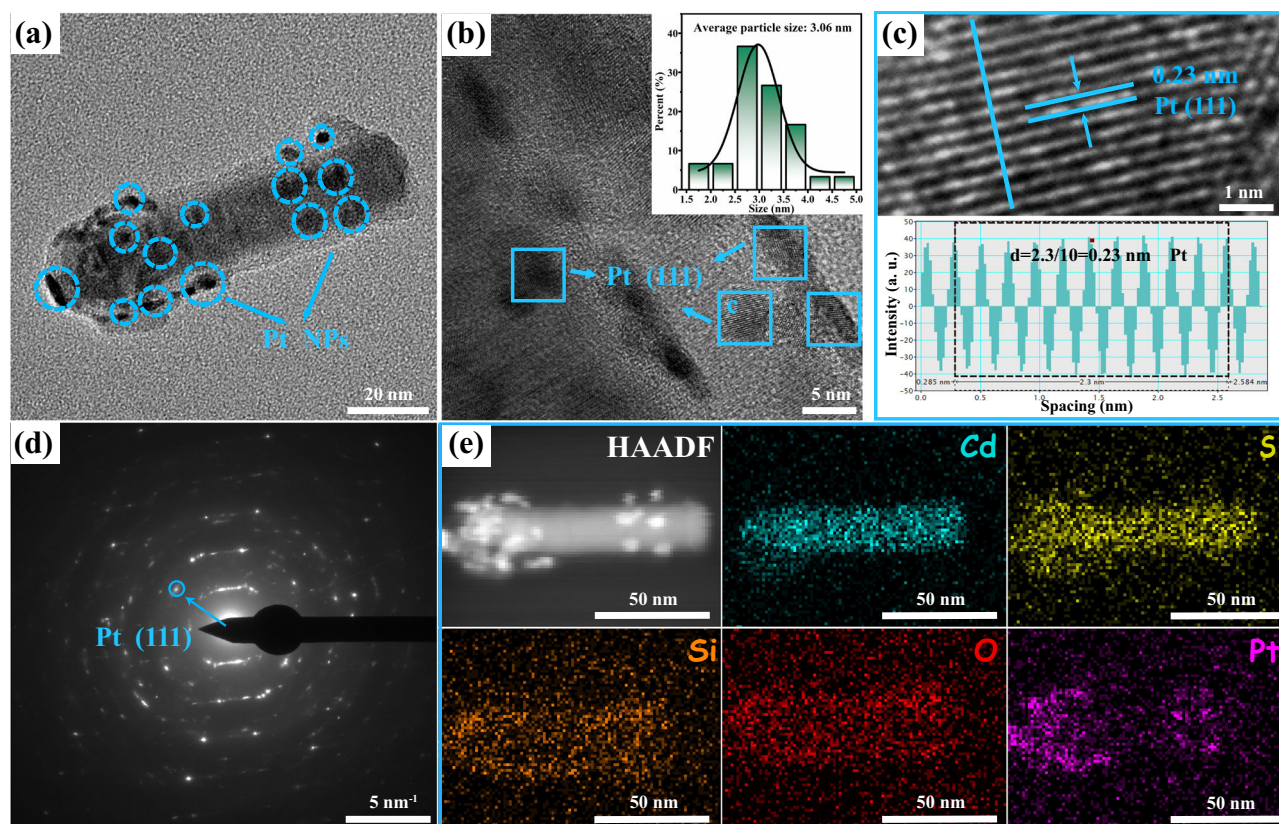
Fig. 2 | The topology of CdS@SiO$_2$-Pt photocatalyst. a TEM images of CdS@SiO$_2$-Pt$_{6.28\%}$ composite photocatalyst. **b** HRTEM image, (**d**), SAED pattern, (**e**), HAADF image and EDX mappings of CdS@SiO$_2$-Pt$_{6.28\%}$ composite photocatalyst. Inset of (**b**) is the particle size distribution of Pt NPs on the surface of CdS@SiO$_2$-Pt$_{6.28\%}$ composite photocatalyst. **c** Partial magnification of (**b**) and corresponding line profile of selected area.

provide the evidences for this conclusion. Obviously, the CdS@SiO$_2$ composite still appears nanorod-like morphology with smooth surface and increased transverse size (Supplementary Fig. 3), and the lattice fringes of $d = 0.32$ nm in Supplementary Fig. 4a, b are assigned to the (101) crystal plane of hexagonal CdS[25]. After SiO$_2$ coverage, a nanolayer with a thickness of ~4.86 nm can be clearly observed from the inset of Fig. 1c, forming a typical core-shell nanorod structure. As shown in Fig. 1d, compared with the bare CdS NRs (0.84 mmol g^{-1} h^{-1}), a slight decrease of SSL-driven HTH rate (0.84 → 0.63 mmol g^{-1} h^{-1}) is presented on CdS@SiO$_2$ NRs, which ascribes to the inactive character of SiO$_2$ nanolayer in HTH conversion. However, the unconspicuous photoactivity decrease indicates that the photoexcitons of internal CdS NRs can easily pass through the SiO$_2$ nano-barrier to participate in surface reaction owing to the quantum tunneling effect of photoexcitons[26,27].

Subsequently, in order to ensure the successful immobilization of Pt NPs on the surface of CdS@SiO$_2$ NRs, its surface was amino-functionalized using 3-aminopropyl triethoxysilane (APTES). FTIR spectrum in Supplementary Fig. 1 shows obviously enhanced absorption peak assigned to the stretching vibration of N-H bonds at 3444 cm^{-1} [20], demonstrating the successful amino-functionalization of CdS@SiO$_2$ NRs. Then, Pt NPs was immobilized on the surface of core-shell CdS@SiO$_2$ NRs through the complexation of amino groups and Pt^{4+} ions following a chemical reduction (NaBH$_4$), and it can be clearly observed from the TEM and HRTEM images in Fig. 2a, b that a large number of well-dispersed nanoparticles with an average size of ~3 nm appear on the surface of SiO$_2$ nanolayer. The lattice fringes ($d = 0.23$ nm) and diffraction spots assigned to the (111) crystal plane of face-centered cubic (fcc) phase Pt can be observed from the enlarged HRTEM image of Fig. 2c and selected area electron diffraction pattern of Fig. 2d[28,29], and the nanoparticles can be further

identified as Pt NPs from the energy dispersive X-ray mapping of Fig. 2e. Therefore, it proves the successful immobilization of Pt NPs on the surface of CdS@SiO$_2$ NRs. Moreover, the loading capacity of Pt NPs on CdS@SiO$_2$ NRs was regulated by changing the dosage of K$_2$PtCl$_6$, so a series of CdS@SiO$_2$-Pt photocatalysts were prepared. The actual Pt loading capacities were determined as 3.53%, 6.28%, and 9.68% by ICP-MS technique, and the corresponding samples were represented as CdS@SiO$_2$-Pt$_{3.53\%}$, CdS@SiO$_2$-Pt$_{6.28\%}$ and CdS@SiO$_2$-Pt$_{9.68\%}$, respectively. Accordingly, with the increase of loading capacity of Pt NPs, the partially magnified XRD patterns in Fig. 1b appear gradually increased diffraction peak assigned to the (111) crystal plane of fcc phase Pt (PDF#87-0647) at $2\theta = 39.9°$[30], which is consistent with the result of inductively coupled plasma mass spectrometer (ICP-MS) analysis. Figure 1d shows that loading Pt NPs on the surface of CdS@SiO$_2$ NRs can effectively improve its SSL-driven HTH photoactivity in alkaline condition, which determines that the photoelectrons of internal CdS NRs can easily transfer to the surface Pt NPs through the SiO$_2$ nano-barrier under photoirradiation. With the dosage increase of Pt NPs, the SSL-driven HTH rates of CdS@SiO$_2$-Pt composite photocatalysts show a trend of first increasing and then decreasing (2.98 → 6.24 → 4.47 mmol g^{-1} h^{-1}). When the loading capacity of Pt NPs is too low (e.g., CdS@SiO$_2$-Pt$_{3.53\%}$, Supplementary Fig. 5a), the number of Pt NPs as the active sites is very small, so its ability to accept photoelectrons from internal CdS NRs is very limited, resulting low photoactivity. On the contrary, when the loading capacity of Pt NPs is too high (e.g., CdS@SiO$_2$-Pt$_{9.68\%}$, Supplementary Fig. 5b), excess Pt NPs is easy to aggregate to form agglomerates due to the high surface energy, which significantly reduces the exposed quantity of active sites, resulting destroyed synergistic effect of cocatalyst and reducing the HTH photoactivity. Especially, the highest SSL-driven HTH rate
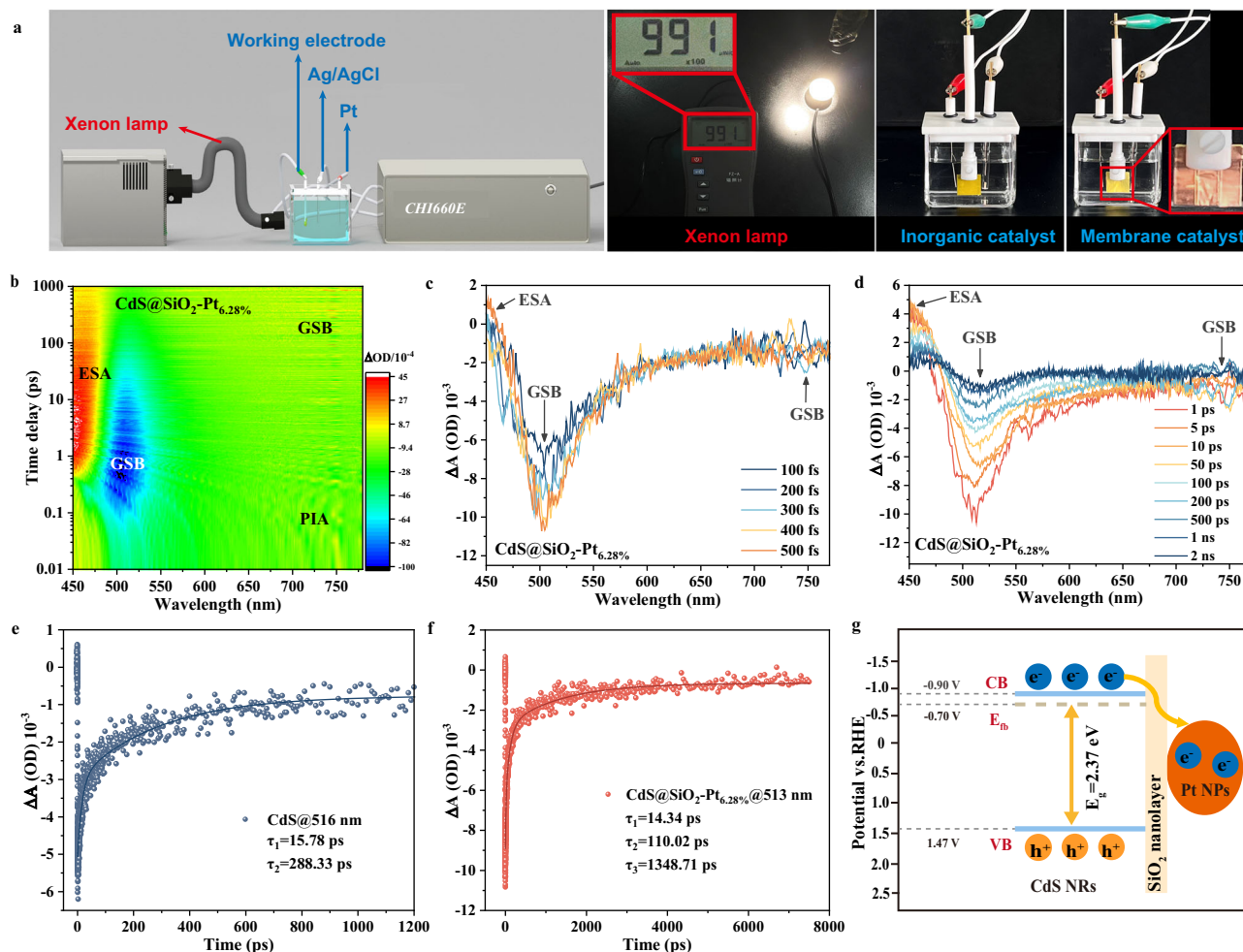
Fig. 3 | The photoelectric properties and exciton dynamics of inorganic catalyst. a Schematic diagram of the three-electrode electrochemical test system, light density (99.1 mW·cm^{-2}) of the irradiated light source and the working electrodes of inorganic catalyst and membrane catalyst. **b** 2D mapped TA spectra, (**c**), TA spectra, (**d**), attenuated TA spectra of CdS@SiO$_2$-Pt$_{6.28\%}$ composite photocatalyst. **e, f** Decay kinetic curves of CdS NRs and CdS@SiO$_2$-Pt$_{6.28\%}$ composite photocatalyst. **g** Band structure of CdS@SiO$_2$-Pt$_{6.28\%}$ composite photocatalyst. The fs-TA tests were performed under excitation of a 380 nm-pump pulse.

(6.24 mmol g^{-1} h^{-1}) was achieved by CdS@SiO$_2$-Pt$_{6.28\%}$ composite photocatalyst, which is about 7.4-fold greater of bare CdS NRs. Its high-resolution Pt 4 f X-ray photoelectron spectroscopy (XPS) spectrum in Supplementary Fig. 2c shows two characteristic peaks assigned to Pt 4$f_{7/2}$ (69.68 eV) and Pt 4$f_{5/2}$ (73.12 eV) electron orbitals of Pt^0, respectively[31], indicating that Pt NPs were immobilized on the surface of CdS@SiO$_2$ NRs in zero-valence state.

Photoelectric properties of inorganic catalyst

The photoelectric property play an important role in determining the catalytic performance of photocatalysts. UV-Vis absorption spectra in Supplementary Fig. 6 shows that the maximum absorption edge (λ_{max}) of bare CdS NRs blue-shifts to 527 nm from 540 nm after coating SiO$_2$ nanolayer, which is attributed to the non-optical response feature of SiO$_2$ coating. Due to the quantum size of SiO$_2$ nanolayer, the λ_{max} of CdS@SiO$_2$ NRs is very close to bare CdS NRs, and excellent visible-light harvesting capacity is still maintained. Further immobilizing Pt NPs on the surface, obviously red-shifted λ_{max} is observed (527 nm→563 nm), and its absorption capacity is also enhanced significantly in broadband light range (λ > 510 nm), which is attributed to the optical enhancement of synergetic host (CdS)-guest (Pt) interaction[32] and surface plasmon resonance effect of Pt NPs[33,34]. Therefore, the CdS@SiO$_2$-Pt$_{6.28\%}$ composite photocatalyst can be confirmed to possess excellent broadband light harvesting capacity. Furthermore, steady-state

photoluminescence (PL) spectra (λ_{ex} = 380 nm) in Supplementary Fig. 7 shows that coating of SiO$_2$ nanolayer significantly reduces the PL emission intensity of bare CdS NRs, indicating effectively suppressed photoexciton recombination kinetics, which is attributed to the comprehensive influence of quantum tunneling effect of photoelectrons and nano-barrier of SiO$_2$ coating. After anchoring Pt NPs, the PL emission intensity is further decreased significantly, which ascribes to that Pt NPs with electron-acceptor character[35,36] can rapidly accept photoelectrons tunneling from the internal CdS NRs through SiO$_2$ nanolayer due to lower potential energy, thus greatly suppressing the photoexciton recombination kinetic, and acquiring higher photon utilization efficiency.

All electrochemical data were tested on a light-assisted three-electrode system (Fig. 3a). Light-induced electrochemical impedance spectroscopies (EIS) in Supplementary Fig. 8 show slightly increased interfacial impedance of CdS NRs due to the coating of SiO$_2$ nanolayer, but it further decreases significantly with immobilization of Pt NPs. This result powerfully proves that photoexcitons in CdS@SiO$_2$-Pt$_{6.28\%}$ composite photocatalyst can easily cross SiO$_2$ nanolayer from internal CdS NRs to the surface Pt active sites due to its quantum tunneling effect. Furthermore, transient photocurrent-time curves in Supplementary Fig. 9 display the intensity trend of CdS@SiO$_2$ < CdS < CdS@SiO$_2$-Pt$_{6.28\%}$, which is basically consistent with the results of UV-Vis absorption spectra and EIS analysis. On the one hand, the SiO$_2$

nanolayer does not significantly affect the photoexciton separation kinetics of CdS NRs under photoirradiation. On the other hand, the electron donor (CdS)-electron acceptor (Pt) interaction greatly promotes the photoelectron migration from internal CdS NRs to surface Pt active sites through the SiO_2 nano-barrier, making the catalyst surface a main area for enriching photoelectrons[37]. In fact, it can be found from the light-induced linear sweep voltammetry curves of Supplementary Fig. 10 and Tafel polarization curves of Supplementary Fig. 11 that the CdS@SiO_2-Pt$_{6.28\%}$ composite photocatalyst shows lower onset potential (0.91 V vs. -2 mA cm^{-2}) and smaller polarized overpotential (917 mV) for photoelectrochemical hydrogen evolution compared with CdS NRs and CdS@SiO_2 NRs, which provides the powerful evidences for the faster HTH kinetics[24].

Exciton dynamics and band structure of CdS@SiO_2-Pt$_{6.28\%}$ composite photocatalyst

Femtosecond transient absorption (fs-TA) spectroscopy technique was adopted under excitation of a 380 nm-pump pulse to investigate the exciton dynamics of the optimal CdS@SiO_2-Pt$_{6.28\%}$ composite photocatalyst. The two-dimensional (2D) mapped TA spectra of CdS NRs and CdS@SiO_2-Pt$_{6.28\%}$ composite photocatalyst display obvious excited state absorption (ESA) signal at 457 nm (Supplementary Fig. 12a and Fig. 3b), which ascribes to the generation of hot excitons in CdS NRs after excitation[38]. Compared with CdS NRs, the CdS@SiO_2-Pt$_{6.28\%}$ composite photocatalyst shows a slightly blue-shifted ground state bleaching (GSB) signal (516 nm→513 nm), indicating that it is easier to reach the excited state under the same excitation[39], which is attributed to the synergistic host (CdS NRs)-guest (Pt NPs) electronic interaction. Supplementary Fig. 12b, c and Fig. 3c, d are the TA spectra of CdS NRs and CdS@SiO_2-Pt$_{6.28\%}$ composite photocatalyst at different relaxation times. It is obvious that the TA intensity of GSB peak increases rapidly in fs range (500 fs) after photoexcitation, and it decreases gradually in subsequent picosecond (ps) and nanosecond (ns) ranges, which ascribes to the instantaneous generation and subsequent recombination of excitons[40]. Comparatively, the maximum TA intensity of CdS@SiO_2-Pt$_{6.28\%}$ composite photocatalyst is stronger than that of bare CdS NRs, indicating that more hot excitons are generated under same excitation[40]. Furthermore, a new GSB signal (~740 nm) can be observed from the TA spectra in relaxation time range of 1–200 ps (Fig. 3c), corresponding to its 2D mapped TA spectrum, which is attributed to the CdS NRs-to-Pt NPs hot electron transfer through SiO_2 nanolayer[41]. Moreover, compared with bare CdS NRs (Fig. 3e), two fast decay processes ($\tau_1 = 14.43$ ps, $\tau_2 = 110.02$ ps) can be observed in the fitted decay kinetics curve of CdS@SiO_2-Pt$_{6.28\%}$ composite photocatalyst (Fig. 3f). The former is attributed to the CdS NRs-to-Pt NPs electron transfer through SiO_2 nanolayer, while the latter indicates the faster conduction band (CB)-to-trapping state (TS) electron transfer of CdS@SiO_2-Pt$_{6.28\%}$ composite photocatalyst than CdS NRs. This can be attributed to that the electron-acceptor feature of Pt NPs enables it to quickly accept tunneling electrons from CdS NRs, providing a strong driving force for accelerating exciton transfer[42]. Moreover, CdS@SiO_2-Pt$_{6.28\%}$ composite photocatalyst ($\tau_3 = 1348.71$ ps) has a longer hot exciton decay lifetime than bare CdS NRs ($\tau_2 = 288.33$ ps), demonstrating that the rapid CdS NRs-to-Pt NPs charge transfer ability greatly restrains the photoexciton recombination kinetics[43].

The flat-band potential of CdS NRs can be determined as $E_{fb(Ag/AgCl)} = -1.31$ V according to its Mott-Schottky curves at different frequencies (Supplementary Fig. 13), and it can be further converted to -0.70 V vs. reversible hydrogen electrode (RHE) potential by following our previous method[24]. Since all the linear parts of Mott-Schottky curves show a positive slope, the E_{CB} of CdS NRs can be determined as $E_{CB(RHE)} = -0.90$ V due to the n-type semiconductor characteristic. Furthermore, its bandgap can be determined as $E_g = 2.37$ eV from the $(ahv)^{n/2}$ ~ hv pattern in Supplementary Fig. 14, thereby its valence band

position can be confirmed to be $E_{VB(RHE)} = 1.47$ V. The specific calculation formulas are given in Supplementary Information. Due to the lower chemical potential of surface Pt NPs, the band structure of CdS@SiO_2-Pt$_{6.28\%}$ composite photocatalyst can be proposed as Fig. 3g.

Membrane catalyst and its comprehensive performance

In order to overcome the drawback of particulate photocatalyst in actual application, the optimal inorganic photocatalyst was compounded with organic ferroelectric PDVF to process into organic-inorganic membrane via a electrospinning technique (Fig. 4a, b). Scanning electron microscope (SEM) images in Fig. 4c show that this membrane is composed by abundant fibers exposing a large number of inorganic materials (Fig. 4d), which benefits to the expose of active sites. As shown in Fig. 4e, pure PVDF membrane can not drive HTH conversion under SSL-irradiation, while all PVDF/CSP membrane catalysts show prominent SSL-driven HTH photoactivity. Moreover, the expose of inorganic catalyst can be well regulated by adjusting its dosage (Supplementary Fig. 15a–f), so as to further control the number of active sites on organic-inorganic matrix. However, it is obvious that excessive inorganic catalyst leads to the aggregation in organic matrix (Supplementary Fig. 15f) due to the uneven dispersion, which will break the synergistic interaction of organic-inorganic interface. Therefore, with the dosage increase of inorganic catalyst, the photoactivities of membrane catalysts showed a trend of increasing first and then decreasing (Fig. 4e). Especially, when the dosage of inorganic catalyst was 0.14 g, the membrane catalyst (PVDF/CSP$_{0.14}$) achieved the highest HTH rate (160.98 mmol m^{-2} h^{-1}), and it further reached to 213.48 mmol m^{-2} h^{-1} and acquired 0.68% of STH efficiency by regulating the thickness of membrane catalyst (Fig. 4f), which considerably outperforms the existing membrane photocatalysts (Table 1)[44–49].

The micro-structural variation and mass loss of particulate catalyst in cyclic process inevitably affect its photoactivity[50,51]. Satisfyingly, the PVDF networked membrane catalyst (PVDF/CSP$_{0.14}$) with synergistic organic-inorganic interface maintained a highly stable photoactivity in 50 cycles (Fig. 4g) due to its high structural stability and convenient separation/recovery property. Owing to the limitation of experimental period (hundreds of hours), the photoactivity may still maintain satisfactory stability even continuously increasing the cyclic number. In addition, the photocurrent response remained stable under long-term (5 h) photoirradiation (Supplementary Fig. 16), which also fully illustrates the excellent light stability and well supports the claim of maintaining highly stable photoactivity over 50 cycles. FTIR spectra in Supplementary Fig. 17 shows that the recovered PVDF/CSP$_{0.14}$ membrane catalyst still display obvious α, β and γ phase characteristics assigned to ferroelectric PVDF[52] even being reused dozens of times, and the digital photos and SEM images in Fig. 4h also did not appear obvious variation in the appearance and micromorphology after 50-times of cycles, suggesting the strong regenerability. Therefore, it indicates that the drawback of particulate catalyst in long-term photo-activation was dramatically overcome to better meet practical application. Stress-strain curves in Supplementary Fig. 18 indicate that the compound of inorganic particulate catalyst significantly increase the tensile strength (3.34 MPa→4.11 MPa) and tensile elongation yield (0.65% → 0.88%) of PVDF membrane, suggesting significantly enhanced mechanical strength. Meanwhile, the PVDF/CSP$_{0.14}$ membrane catalyst possesses smaller interfacial impedance than pure PVDF membrane (Supplementary Fig. 19), indicating that the formation of synergistic organic-inorganic interface significantly promotes exciton transfer. Based on the superior broadband light harvesting capacity of inorganic catalyst and piezoelectric effect of PVDF matrix, the PVDF/CSP$_{0.14}$ membrane catalyst appears stronger response current signals under transient induction of photoirradiation (Supplementary Fig. 20) or ultrasound (Supplementary Fig. 21) than pure PVDF membrane, suggesting the potential of photo-activation and piezoelectric activation. The strong piezoelectric current and
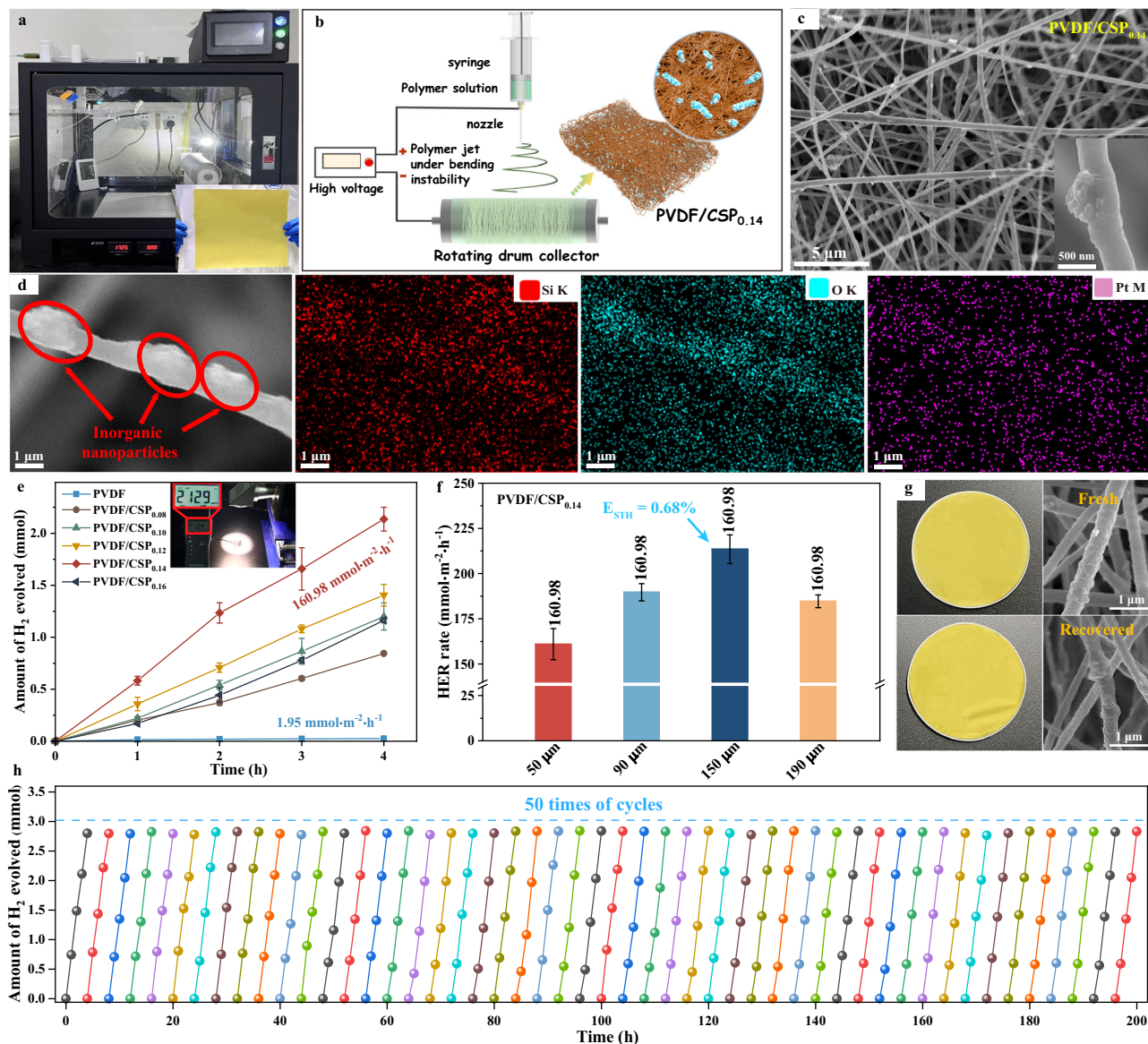
Fig. 4 | The membrane catalyst and its comprehensive performance. a Digital photo of electrospinning equipment. **b** Schematic diagram of electrospinning technique. **c** SEM image and (**d**), EDS mappings of PVDF/CSP$_{0.14}$ membrane catalyst. Inset of (**c**) is the partial magnification. Inset of (**e**) is the light density (212.9 mW·cm^{-2}) used in HTH performance evaluation. Error bars in (**e**, **f**) indicate the standard deviation for three measurements.
e HTH performances of membrane catalysts with different dosage of inorganic catalyst (0 g → 0.16 g) and (**f**), different thickness (50 μm → 190 μm). **g** Cyclic HTH performances of PVDF/CSP$_{0.14}$ membrane catalyst. **h** Digital photos and SEM images of fresh and recovered PVDF/CSP$_{0.14}$ membrane catalyst. Inset of (**a**) is the digital photo of PVDF/CSP$_{0.14}$ membrane catalyst with the size of 21 cm × 24 cm.

voltage signals in Supplementary Fig. 22a, b and the obvious performance advantage of PVDF/CSP$_{0.14}$ membrane catalyst than the non-ferroelectric composite membrane (polyurethane (PU)/VSP$_{0.14}$) in Supplementary Fig. 23 provide the direct evidences to this conclusion.

Panel water-splitting reaction system and photocatalytic mechanism

Subsequently, a homemade panel water-splitting reaction system was fabricated as Fig. 5a Alkaline water (pH = 14.0) flowed into the panel reaction module embedded membrane catalyst (16 cm × 23 cm) at a flow rate of 20 mL/min under driving of peristaltic pump. When the panel reaction module is filled, it was irradiated by a xenon lamp to drive water splitting. Water-gas mixture flowed into a gas-liquid separation bottle from panel reaction module, and gaseous product was dried in a drying bottle containing concentrated sulfuric acid and subsequently entered a gas collecting bottle as

Fig. 5b. As shown as the inset of Fig. 5a and supplemented Supplementary Movie 1, it can be observed from the panel reaction module that a large number of bubbles are continuously evolved on the surface of membrane catalyst under SSL-irradiation. With continuous reaction, bubbles were released in drying bottle (Fig. 5c), and supplemented Supplementary Movie 2 provides direct evidence for this phenomenon. After 3 h of reaction, gas sample was extracted from the sampling port of gas collecting bottle for gas chromatographic detection, and chromatographic peaks belonging to hydrogen and oxygen appeared as Fig. 5d, e, indicating the successful progress of water splitting process in this panel reaction system. The ignition experiment of collected gas in inset of Fig. 5e and Supplementary Movie 3 further provides the evidence for this conclusion, and 0.05% of STH efficiency was achieved on this panel reaction system for water splitting. Due to the high stability of this membrane catalyst, no active catalyst lost from the panel reaction

Table 1 | HTH performance contrast of PVDF/CSP$_{0.14}$ membrane catalyst with other reported membrane catalysts

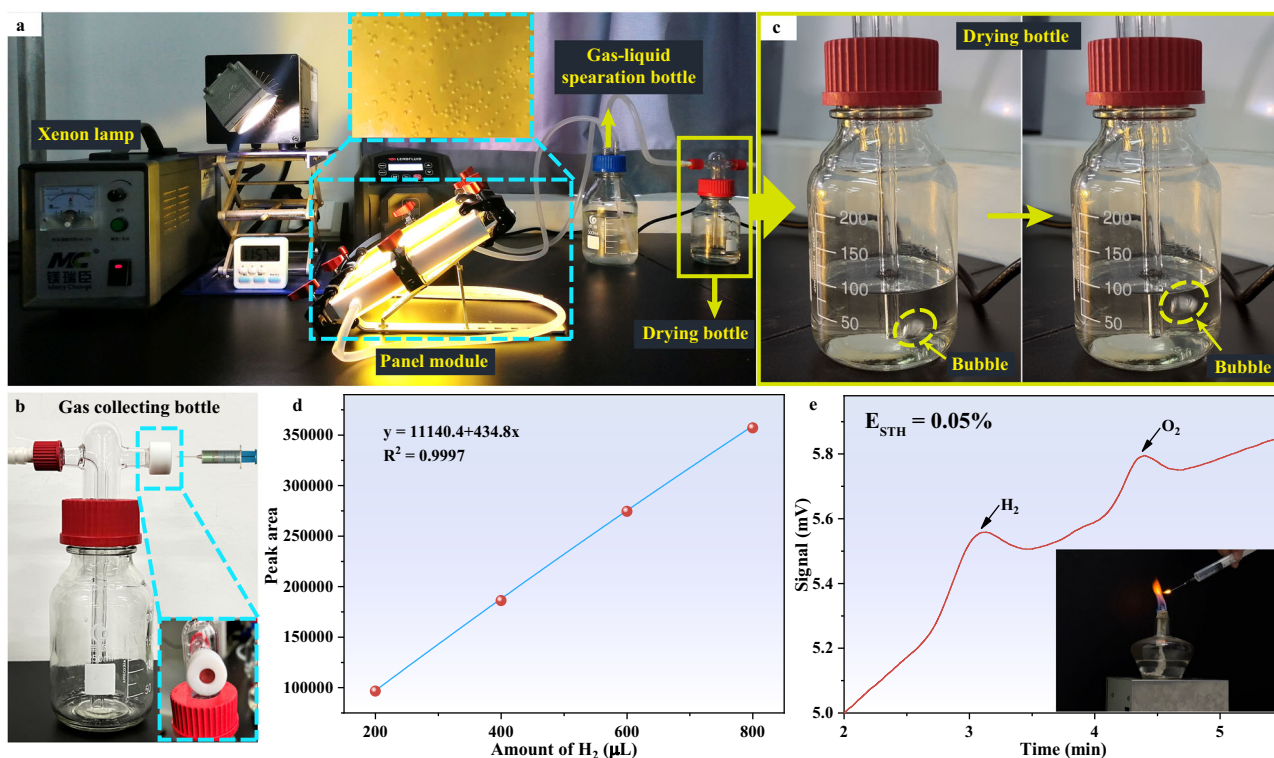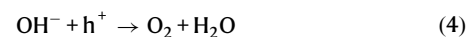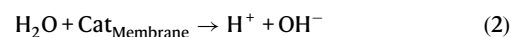| Entry	Catalyst	HTH rate (mmol·m^{-2}·h^{-1})	STH efficiency (%)	Stability	Refs.
1	TiO$_x$/CoOOH/Rh/SrTiO$_3$	/	0.4	>100 h	44
2	g-C$_3$N$_4$/LiNbO$_3$/PVDF	1.016×10^{-2}	/	/	45
3	Pt$_{0.3}$-ZIS	43.17	/	>50 h	46
4	Cu-SA/TiO$_2$ NPs	11.3	/	>3 times	47
5	CTFs film	5.4	/	>100 h	48
6	SVG-PC	17.8	0.13	>154 h	49
7	PVDF/CSP$_{0.14}$	213.48	0.68	>200 h	This work

Fig. 5 | The panel water-splitting reaction system and photocatalytic mechanism. a Digital photos of laboratorial panel reaction system based on the membrane catalyst: **b** gas collecting bottle and (**c**), bubble display in gas drying bottle. **d** Hydrogen standard curve obtained on a gas chromatograph (FULI, GC 9790II, CN). **e** Gas chromatogram of gaseous product from this panel reaction system.

module even suffering long-term mechanical forces of fluid flow and bubble collision. By increasing the number of panel modules, the scale of panel reaction system can be expanded as Supplementary Fig. 24, so that water splitting can be achieved under strong outdoor solar-irradiation. Of course, there are still many engineering problems to be solved in actual operation. Based on our study, the catalytic mechanism of this membrane catalyst for HTH conversion is proposed as Supplementary Fig. 25. Owing to the excellent broadband light-harvesting capacity of inorganic catalyst and sensitive piezoelectricity of PVDF matrix, the membrane catalyst in panel reaction module can be double-activated under stimulations of light energy and mechanical energy, thus generating high-density excitons $(e^- + h^+)$ to drive HTH conversion (**1**). Due to the presence of hydroxyl groups on the surface of SiO$_2$ nanolayer and the influence of a large number of OH$^-$ ions in aqueous phase, a low chemical potential conducive to the transfer of photogenerated h^+ from CdS NRs to the surface of SiO$_2$ nanolayer is formed, and related oxidation reactions can be achieved on the surface of the catalytic material, effectively avoiding the impact of corrosion on the internal CdS microstructure. The relevant processes are shown

as follows: (**1**)-(**4**). In this catalytic process, OH$^-$ ions consume most of the photogenerated h^+ (**4**), thus better promoting the half-reaction of hydrogen production (**3**).

$$Cat_{Membrane} + h\nu \rightarrow Cat_{Membrane}(e^- + h^+) \quad (1)$$

$$H_2O + Cat_{Membrane} \rightarrow H^+ + OH^- \quad (2)$$

$$H^+ + e^- \rightarrow H_2 \quad (3)$$

$$OH^- + h^+ \rightarrow O_2 + H_2O \quad (4)$$

In summary, in order to overcome the drawback of particulate photocatalysts in flat-panel HTH conversion, a highly active CdS@SiO$_2$-Pt composite with rapid CdS-to-Pt electron-transfer kinetics and restrained photoexciton recombination kinetics was prepared to process into an organic-inorganic membrane by compounding with

organic ferroelectric PVDF. This PVDF networked membrane catalyst with synergistic organic-inorganic interface displays high photostability and excellent operability, achieving improved SSL-driven alkaline (pH = 14.0) HTH activity (213.48 mmol m^{-2} h^{-1}) following a 0.68% of STH efficiency. No obvious variation in its appearance and micromorphology was observed even being recycled for 50-times, which considerably outperforms the existing membrane photocatalysts. Subsequently, a homemade panel reaction system was fabricated to achieve alkaline water-splitting to obtain a 0.05% of STH efficiency under SSL-irradiation. This study opens up a prospect for practical application of panel photocatalytic hydrogen production with organic-inorganic interface networked membrane technology.

Methods

All chemical reagents used in this study were purchased from Sinopharm Group Chemical Reagents Co., LTD without any purification treatment.

Preparation of core-shell CdS@SiO$_2$ NRs and its surface amino-functionalization

The CdS NRs were hydrothermally synthesized by following our previous protocol[25], and the detailed procedure is given in Supplementary Information. The CdS@SiO$_2$ NRs were prepared by coating a SiO$_2$ nanolayer on the surface of CdS NRs via a sol-gel method (Fig. 1a). Specifically, 0.3 g CdS NRs was ultrasonically dispersed in a mixed solution of 20 mL deionized water and 40 mL absolute ethanol (A.R.), and the dispersion was magnetically agitated for 15 min after adding 1 mL NH$_3$·H$_2$O (25 wt%). Then, 2 mL tetraethoxysilane (TEOS, A.R.) was added to this mixture drop by drop following a 6 h of magnetic agitation at room temperature. After the reaction, the product was centrifuged and rinsed for several times with deionized water, and powdered CdS@SiO$_2$ NRs was obtained after heat drying at 80 °C.

Amino-functionalization of core-shell CdS@SiO$_2$ NRs was achieved through the bonding interaction between silane coupling agent and silicon hydroxyl group. 1 g CdS@SiO$_2$ NRs was ultrasonically dispersed in 50 mL acetone (A.R.), and 1 mL APTES (A.R.) and 2 drops of NH$_3$·H$_2$O (25 wt%) were added to this dispersion following a 3 h of magnetic agitation at 50 °C under reflux condensation. After the reaction, the sample was centrifuged and rinsed for several times with ethanol and deionized water, and amino-functionalized CdS@SiO$_2$ NRs (CdS@SiO$_2$-NH$_2$) was obtained after heat drying at 80 °C.

Preparation of CdS@SiO$_2$-Pt composite photocatalyst

The Pt NPs was immobilized on the surface of core-shell CdS@SiO$_2$ NRs through the complexation of surface amino groups and Pt^{4+} ions following a reduction process (Fig. 1a). 0.1 g as-prepared CdS@SiO$_2$-NH$_2$ and 0.01 g K$_2$PtCl$_6$ (A.R.) were added to 25 mL deionized water for 30 min of magnetic agitation, and 10 mL deionized water dissolving appropriate amount of NaBH$_4$ (A.R.) was added to this mixture by drops. After 2 h of continuous agitation, the sample was collected and rinsed for several times with deionized water, and CdS@SiO$_2$-Pt composite photocatalyst was obtained after heat drying at 80 °C. In this process, the amount of Pt NPs in composite can be precisely regulated by adjusting the dosage of K$_2$PtCl$_6$, thus to prepare a series of CdS@SiO$_2$-Pt composite photocatalysts with different Pt dosages. The actual Pt loading capacities were determined on an inductively coupled plasma mass spectrometer (ICP-MS, ICPA 6000 SERIES, USA).

Processing of PVDF/CSP membrane catalyst

The PVDF/CSP membrane catalyst was processed via an electrospinning technique by compounding the optimal inorganic photocatalyst with PVDF. Concretely, 0.5 g PVDF powder ($\bar{M}$ = 500 thousands) was dissolved in a mixed solvent of 3.36 mL DMF (A.R.) and 2.24 mL acetone (A.R.), and a certain amount of inorganic photocatalyst was ultrasonically dispersed in this polymer solution. The precursor

mixture for electrospinning was prepared after 30 min of agitation at 40 °C, and the uniform mixture was transferred to a syringe with a volume of 10 mL and sprayed at a steady flow rate of 1 mL h^{-1} and a potential of 9.32 kV through a 0.6 mm needle. The rotating speed of collecting drum was 200 rpm, which is 15 cm from the needle, and the moving speed of sliding platform was 32 mm s^{-1}. After 4 h of spinning and 2 h of heat drying at 60 °C, the PVDF/CSP membrane catalyst with a size of 21 cm × 24 cm was obtained. In this process, a series of membrane catalysts were processed by adjusting the amount of inorganic photocatalyst, and the resultant materials were expressed as PVDF/CSP$_\alpha$ (Here, α represents the mass of inorganic photocatalyst in membrane catalyst). Meanwhile, the bare PVDF membrane was prepared for contrast by the same procedure at absence of inorganic photocatalyst. In addition, the PVDF powder was replaced by PU powder to process the PU/CSP membrane catalyst for contrast by the same operation.

Characterization

The crystal structures of the samples were analyzed on a powder X-ray diffractometer (XRD, D8 Advance, GER). Fourier transform infrared spectrometer (FTIR, Bruker Alpha VECTOR 22, GER) and X-ray photoelectron spectrometer (XPS, AXIS SUPRA, UK) were performed to analyze the chemical structure, elemental composition and chemical states of the samples. The topology and crystallography of the samples were observed on a field emission transmission electron microscope (TEM, FEI Tecnai G2 F30 S-TWIN, USA) and field emission scanning electron microscopy (SEM, SU8100, Japan). UV-Vis absorption spectra were measured on a UV-Vis-NIR spectrophotometer (Agilent, Cary 5000, USA), and steady-state photoluminescence (PL) spectra were measured on a fluorescence spectrometer (Edinburgh FLS980, UK), and the excitation wavelength (λ_{ex}) and emission wavelength (λ_{em}) was set as 380 nm and 544 nm, respectively. Femtosecond transient absorption (fs-TA) spectroscopy was performed to investigate the exciton dynamics utilizing a coherent legend laser system equipped a home-modified Helios (ultrafast) device. This measurement involved in an 800 nm of laser (2840 mW) emitting from a seed source through a titanium sapphire amplifier, and the pulse frequency and time interval are 1000 Hz and 75 fs, respectively.

SSL-driven alkaline HTH photoactivity evaluation

The HTH photoactivity was evaluated on a Labsolar-III AG system of Beijing Perfectlight Technology Co., Ltd. equipped with a 300 W xenon lamp (MC-PF300C, 212.9 mW·cm^{-2}) and a gas chromatograph (FULI, GC 9790II, CN) by using high purity nitrogen as carrier gas. All error bars were determined according to three measurements.

For inorganic photocatalysts, 50 mL deionized water uniformly dispersing 10 mg catalyst was added to a closed glass photoreactor after regulating the pH value to 14.0 with 0.1 M NaOH solution. After 10 min of degassing treatment, it was photoirradiated for 4 h under magnetic agitation, and sampling and detecting were performed every 1 h to determine the amount of hydrogen by comparing with its standard curve in Supplementary Fig. 26.

For membrane catalysts, a circular membrane catalyst with a diameter of 6.5 cm was cut to replace the inorganic particulate photocatalyst and fixed in the closed glass photoreactor to perform the HTH conversion, and the membrane catalyst was impregnated 0.3 cm below the liquid level in photocatalytic process. After the reaction, the membrane was collected and rinsed several times with deionized water to achieve its regeneration for next reuse. All cyclic experiments were performed using the same operation.

Calculation of STH efficiency

The STH efficiency of the optimal membrane catalyst for SSL-driven alkaline HTH conversion was calculated using the method reported in

literature[49,53], and the specific calculation method is as follows:

$$STH(\%) = \frac{Energy\ output\ asH_2}{Incident\ solar\ light\ energy}$$
$$= \left(R_{H_2} \times \triangle G^0\right)/(P \times S) \times 100 \qquad (5)$$

where R_{H_2} represents the HTH rate (1.99×10^{-7} mol·s^{-1}), $\triangle G^0$ represents its standard Gibbs free energy (237.13×10^3 J mol^{-1} at 298 K), P represents the light intensity of irradiated light (212.9 mW cm^{-2}), and S represents the illuminated area (33.17 cm^2).

Photoelectric property tests

All photoelectric data was detected on an electrochemical workstation (CHI 660E, CN) equipped a 350 W xenon lamp (BBZM-III, CN, 99.1 mW cm^{-2}, Fig. 3a), and a three-electrode system composed of working electrode, counter electrode (Pt electrode) and reference electrode (Ag$^+$/AgCl electrode) was installed in a quartz groove containing 0.2 M Na$_2$SO$_4$ electrolyte (pH = 7). For inorganic catalysts, ITO glasses (15 mm × 15 mm) coated by tested samples were used as the working electrodes[54]. Detailedly, 5 mg tested sample was ultrasonically dispersed into the mixed solution of 3 mL anhydrous ethanol and a drop of naphthol to form a uniform mixture, and it was uniformly coated on the conductive side of the ITO glass through a pipette following a drying treatment in an oven (60 °C). Repeating the above coating and drying operations until the mixed liquid is exhausted completely. For membrane catalysts, 15 mm × 15 mm of square membranes were cut and bonded to a conductive copper adhesive with the same size to get the working electrode for test of photoelectric properties. The specific test parameters were same as that of inorganic catalysts and is provided in Supplementary Information.

Additional information

The synthesis of CdS NRs, parameters for photoelectric property tests, Kubelka-Munk function, calculation formulas for band structure and the supplemented data are contained in Supplemented Information.

Reporting summary

Further information on research design is available in the Nature Portfolio Reporting Summary linked to this article.

Data availability

Source data are provided as a Source Data file. Source data are provided with this paper.

References

1. Lv, J. et al. Solar utilization beyond photosynthesis. *Nat. Rev. Chem.* **7**, 91–105 (2023).
2. Zhao, H. & Yuan, Z.-Y. Progress and perspectives for solar-driven water electrolysis to produce green hydrogen. *Adv. Energy Mater.* **13**, 2300254 (2023).
3. Zhang, Y. et al. Photocatalytic oxidation for volatile organic compounds elimination: from fundamental research to practical applications. *Environ. Sci. Technol.* **56**, 16582–16601 (2022).
4. Zhang, Y. et al. Internal quantum efficiency higher than 100% achieved by combining doping and quantum effects for photocatalytic overall water splitting. *Nat. Energy* **8**, 504–514 (2023).
5. Fang, S. et al. Photocatalytic CO$_2$ reduction. *Nat. Rev. Methods Prim.* **3**, 61 (2023).
6. Xiong, Y. et al. Photocatalytic nitrogen fixation under an ambient atmosphere using a porous coordination polymer with bridging dinitrogen anions. *Nat. Chem.* **15**, 286–293 (2023).
7. Freese, T., Meijer, J. T., Feringa, B. L. & Beil, S. B. An organic perspective on photocatalytic production of hydrogen peroxide. *Nat. Catal.* **6**, 553–558 (2023).
8. Liu, P. et al. Synergy between palladium single atoms and nanoparticles via hydrogen spillover for enhancing CO$_2$ photoreduction to CH$_4$. *Adv. Mater.* **34**, 2200057 (2022).
9. Das, R. et al. Engineering the charge density on an In$_{2.77}$S$_4$/porous organic polymer hybrid photocatalyst for CO$_2$-to-ethylene conversion reaction. *J. Am. Chem. Soc.* **145**, 422–435 (2023).
10. Guo, X. et al. A sustainable wood-based iron photocatalyst for multiple uses with sunlight: water treatment and radical photopolymerization. *Angew. Chem. Int. Ed.* **62**, e202301242 (2023).
11. Hisatomi, T. & Domen, K. Reaction systems for solar hydrogen production via water splitting with particulate semiconductor photocatalysts. *Nat. Catal.* **2**, 387–399 (2019).
12. Nishiyama, H. et al. Photocatalytic solar hydrogen production from water on a 100-m^2 scale. *Nature* **598**, 304–307 (2021).
13. Zhou, P. et al. Solar-to-hydrogen efficiency of more than 9% in photocatalytic water splitting. *Nature* **613**, 66–70 (2023).
14. Li, X. et al. Recent advances in noncontact external-field-assisted photocatalysis: from fundamentals to applications. *ACS Catal.* **11**, 4739–4769 (2021).
15. Orudzhev, F. et al. Ultrasound and water flow driven piezo-phototronic effect in self-polarized flexible α-Fe$_2$O$_3$ containing PVDF nanofbers film for enhanced catalytic oxidation. *Nano Energy* **90**, 106586 (2021).
16. Ghosh, R. et al. Exciton manipulation for enhancing photoelectrochemical hydrogen evolution reaction in wrinkled 2D heterostructures. *Adv. Mater.* **35**, 2210746 (2023).
17. Xu, M.-L. et al. Piezo-photocatalytic synergy in BiFeO$_3$@COF Z-scheme heterostructures for high-efficiency overall water splitting. *Angew. Chem. Int. Ed.* **61**, e202210700 (2022).
18. Liu, J. et al. Piezocatalytic techniques in environmental remediation. *Angew. Chem. Int. Ed.* **62**, e202213927 (2023).
19. Ghaffar, A., Zhang, L., Zhu, X. & Chen, B. Porous PVdF/GO nanofibrous membranes for selective separation and recycling of charged organic dyes from water. *Environ. Sci. Technol.* **52**, 4265–4274 (2018).
20. Nagasawa, H. et al. Ultrafast synthesis of silica-based molecular sieve membranes in dielectric barrier discharge at low temperature and atmospheric pressure. *J. Am. Chem. Soc.* **143**, 35–40 (2021).
21. Xu, L. et al. Chiral skeletons of mesoporous silica nanospheres to mitigate alzheimer's β-amyloid aggregation. *J. Am. Chem. Soc.* **145**, 7810–7819 (2023).
22. Chen, Z. et al. Non-oxidative coupling of methane: N-type doping of niobium single atoms in TiO$_2$-SiO$_2$ induces electron localization. *Angew. Chem. Int. Ed.* **60**, 11901–11909 (2021).
23. Ma, Y. et al. Si/SiO$_2$@graphene superstructures for high-performance lithium-ion batteries. *Adv. Funct. Mater.* **33**, 2211648 (2023).
24. Li, W. et al. Promoting body carriers migration of CdS nanocatalyst by N-doping for improved hydrogen production under simulated sunlight irradiation. *Appl. Catal. B-Environ.* **313**, 121470 (2022).
25. Li, W. et al. Nanoconfinement dynamics and crystal plane exposure: synergistic promotion of simulated solar-driven H$_2$O-to-H$_2$ conversion on host (CdS)-guest (Ti single-atom) nano-photocatalyst. *Chem. Eng. J.* **472**, 144793 (2023).
26. Yukawa, R. et al. Resonant tunneling driven metal-insulator transition in double quantum-well structures of strongly correlated oxide. *Nat. Commun.* **12**, 7070 (2021).
27. Aiello, G. et al. Quantum bath engineering of a high impedance microwave mode through quasiparticle tunneling. *Nat. Commun.* **13**, 7146 (2022).
28. Shi, Z. et al. Phase-dependent growth of Pt on MoS$_2$ for highly efficient H$_2$ evolution. *Nature* **621**, 300–305 (2023).
29. Hong, Y.-R. et al. Crystal facet-manipulated 2D Pt nanodendrites to achieve an intimate heterointerface for hydrogen evolution reactions. *J. Am. Chem. Soc.* **144**, 9033–9043 (2022).

30. Li, W. et al. Enhanced cocatalyst-support interaction and promoted electron transfer of 3D porous g-C$_3$N$_4$/GO-M (Au, Pd, Pt) composite catalysts for hydrogen evolution. *Appl. Catal. B-Environ.* **288**, 120034 (2021).

31. Dong, W. J. et al. Pt nanoclusters on GaN nanowires for solar-asssisted seawater hydrogen evolution. *Nat. Commun.* **14**, 179 (2023).

32. Shi, B. et al. Platinum metallacycle-based molecular recognition: establishment and application in spontaneous formation of a [2] rotaxane with light-harvesting property. *Angew. Chem. Int. Ed.* **135**, e202305767 (2023).

33. Wan, P.-K. et al. Platinum(II) N-heterocyclic carbene complexes arrest metastatic tumor growth. *PNAS* **118**, e2025806118 (2021).

34. Wei, D.-Y. et al. In situ Raman observation of oxygen activation and reaction at platinum-ceria interfaces during CO oxidation. *J. Am. Chem. Soc.* **143**, 15635–15643 (2021).

35. Chen, J., Wang, Y., Wang, F. & Li, Y. Photo-induced switching of CO$_2$ hydrogenation pathway towards CH$_3$OH production over Pt@UiO-66-NH$_2$(Co). *Angew. Chem. Int. Ed.* **135**, e202218115 (2023).

36. Xu, D. et al. Boosting mass exchange between Pd/NC and MoC/NC dual junctions via electron exchange for cascade CO$_2$ fixation. *J. Am. Chem. Soc.* **144**, 5418–5423 (2022).

37. Liu, Y., Cullen, D. A. & Lian, T. Slow auger recombination of trapped excitons enables efficient multiple electron transfer in CdS-Pt nanorod heterostructures. *J. Am. Chem. Soc.* **143**, 20264–20273 (2021).

38. Wang, W. et al. Fullerene-graphene acceptor drives ultrafast carrier dynamics for sustainable CdS photocatalytic hydrogen evolution. *Adv. Funct. Mater.* **32**, 2201357 (2022).

39. Li, Y. et al. Revealing the importance of hole transfer: boosting photocatalytic hydrogen evolution by delicate modulation of photogenerated holes. *ACS Catal.* **13**, 8281–8292 (2023).

40. Wu, X.-L. et al. Directional and ultrafast charge transfer in oxygen-vacancy-rich ZnO@single-atom cobalt core-shell junction for photo-fenton-like reaction. *Angew. Chem. Int. Ed.* **135**, e202305639 (2023).

41. Kosco, J. et al. Generation of long-lived charges in organic semiconductor heterojunction nanoparticles for efficient photocatalytic hydrogen evolution. *Nat. Energy* **7**, 340–351 (2022).

42. Dong, C. et al. Size-dependent activity and selectivity of carbon dioxide photocatalytic reduction over platinum nanoparticles. *Nat. Commun.* **9**, 1252 (2018).

43. Chen, Z. et al. Tuning excited state electronic structure and charge transport in covalent organic frameworks for enhanced photocatalytic performance. *Nat. Commun.* **14**, 1106 (2023).

44. Suguro, T. et al. A hygroscopic nano-membrane coating achieves efficient vapor-fed photocatalytic water splitting. *Nat. Commun.* **13**, 5698 (2022).

45. Cui, Y. et al. Fluid-induced piezoelectric field enhancing photocatalytic hydrogen evolution reaction on g-C$_3$N$_4$/LiNbO$_3$/PVDF membrane. *Nano Energy* **99**, 107429 (2022).

46. Shi, X. et al. Protruding Pt single-sites on hexagonal ZnIn$_2$S$_4$ to accelerate photocatalytic hydrogen evolution. *Nat. Commun.* **13**, 1287 (2022).

47. Lee, W. H. et al. Floatable photocatalytic hydrogel nanocomposites for large-scale solar hydrogen production. *Nat. Nanotechnol.* **18**, 754–762 (2023).

48. Hu, X., Zhan, Z., Zhang, J., Hussain, I. & Tan, B. Immobilized covalent triazine frameworks films as effective photocatalysts for hydrogen evolution reaction. *Nat. Commun.* **12**, 6596 (2021).

49. Pornrungroj, C. et al. Hybrid photothermal-photocatalyst sheets for solar-driven overall water splitting coupled to water purification. *Nat. Water* **1**, 952–960 (2023).

50. Xu, L., Liang, H.-W., Yang, Y. & Yu, S.-H. Stability and reactivity: positive and negative aspects for nanoparticle processing. *Chem. Rev.* **118**, 3209–3250 (2018).

51. Martín, A. J., Mitchell, S., Mondelli, C., Jaydev, S. & Pérez-Ramírez, J. Unifying views on catalyst deactivation. *Nat. Catal.* **5**, 854–866 (2022).

52. Su, Y. et al. High-performance piezoelectric composites via β phase programming. *Nat. Commun.* **13**, 4867 (2022).

53. Qi, Y. et al. Unraveling of cocatalysts photodeposited selectively on facets of BiVO$_4$ to boost solar water splitting. *Nat. Commun.* **13**, 484 (2022).

54. Li, W. et al. Construction of core-chell Sb$_2$S$_3$@CdS nanorod with enhanced heterointerface interaction for chromium-containing wastewater treatment. *Small* **19**, 2302737 (2023).

Author contributions
W. Li proposed the experimental concepts, designed the experiments and prepared the paper. W. Li and C. Wang supervised the project. W. Li, W. Duan, G. Liao, F. Gao, Y. Wang, and R. Cui carried out the experiments and conducted the materials characterization. W. Li, C. Wang, and J. Zhao revised the paper. All authors discussed the results and approved the final version of the paper.

Competing interests
The authors declare no competing interests.

Additional information
Supplementary information The online version contains supplementary material available at https://doi.org/10.1038/s41467-024-51183-2.

Correspondence and requests for materials should be addressed to Wei Li or Chuanyi Wang.

Peer review information *Nature Communications* thanks the anonymous reviewers for their contribution to the peer review of this work. A peer review file is available.

Reprints and permissions information is available at http://www.nature.com/reprints

Publisher's note Springer Nature remains neutral with regard to jurisdictional claims in published maps and institutional affiliations.